


**Topological phases in photonic microring lattices with projective symmetry**Yang Liu,<sup>1</sup> Chuang Jiang,<sup>1</sup> Wanting Wen,<sup>1</sup> Yiling Song,<sup>2</sup> Xiaohong Li,<sup>1</sup> Peixiang Lu,<sup>3</sup> and Shaolin Ke<sup>1,\*</sup><sup>1</sup>*Hubei Key Laboratory of Optical Information and Pattern Recognition, Wuhan Institute of Technology, Wuhan 430205, China*<sup>2</sup>*Department of Physics, Wenzhou University, Zhejiang 325035, China*<sup>3</sup>*Guangdong Intelligent Robotics Institute, Dongguan 523808, China* (Received 20 June 2023; revised 25 October 2023; accepted 2 January 2024; published 24 January 2024)

Symmetry plays a key role in classifying topological phases, which can be enriched by the projective symmetry group in the presence of artificial gauge fields (AGFs). Here, we utilize two-dimensional (2D) photonic microring lattices to create three different topological states based on projective symmetry. By engineering link rings, we are able to flexibly manipulate the AGFs and coupling magnitude. As each plaquette carries a  $\pi$  flux, the two translation symmetries of a rectangle microring lattice are projectively represented. By applying different types of dimerization, we tune the spatial space to break translation symmetry and achieve a Möbius topological insulator with twisted edge bands and a graphenelike topological semimetal with flat bands, which we reflect by unique excitation spectra and field distributions. Additionally, by changing the configuration of gauge flux, the mirror and translation operators become anticommutative, leading to the fractal translation of the Brillouin zone. As a result, the band structure of topological edge modes experiences twice the period in momentum space. All results are confirmed by full-wave simulation. Our study has the potential to construct unprecedented photonic topological insulators benefiting from gauge fields.

DOI: [10.1103/PhysRevA.109.013516](https://doi.org/10.1103/PhysRevA.109.013516)**I. INTRODUCTION**

Topological photonics provides an alternative approach to controlling light transport via the topology degree of freedom and it is exploited for developing novel photonic devices that are robust to perturbations [1–11]. Advancing nanofabrication technology has enabled the demonstration of topological insulators [12,13], semimetals [14], high-order states [15,16], and non-Hermitian topology [17–23] in a variety of photonic platforms. Remarkably, symmetry, another important concept of modern physics, plays a crucial role in the classification of topological phases. For example, topological insulators and superconductors are categorized by the tenfold method of Altland-Zirnbauer symmetry classes according to internal symmetries [24], such as time-reversal, particle-hole, and chiral symmetries. This formulation provides a complete Periodic Table to understand symmetry-enriched and symmetry-protected topological phases [25]. Building on this progress, the technique has been extended to the case that is protected by space-group symmetries. These symmetries describe the spatial transformations, like translations, rotations, and reflections, that leave a crystal structure unchanged [26–28]. The application of spatial symmetries yields a richer catalog of topological matters and abundant topological crystalline insulators that have not been reported before, providing a rather comprehensive search for candidate topological materials [29].

However, the traditional definition of crystal symmetry does not involve gauge fields. The recent developed metacrys-

tals enable the possibility of generating artificial gauge fields (AGFs), whereby the crystal symmetries are projectively represented, enriching the classification of topological phases [30–41]. The underlying mechanism relies on the phase accumulated for wave functions that would change the algebra of spatial symmetry operations. Using projective inversion or mirror symmetry, the spinless system can host spinful topological phases under  $Z_2$  gauge fields. In a rectangle lattice, breaking the projective translation symmetries gives rise to novel Möbius topological insulators [42–44] and graphenelike semimetal phases [32,42,45]. In addition, the projective symmetry algebra dramatically lead to the fraction of reciprocal lattice, deforming the Brillouin zone from torus into Klein bottle [46], producing novel topological phases distinct from Chern insulators [43]. The principle of projective symmetry and the enriched topological phases have been demonstrated in acoustic cavities [31,43,47–49]. However, the generation of such phases in photonic systems has not been thoroughly explored due to the simultaneous control required for coupling strength and gauge fields.

In this work, we bridge this gap by proposing that microring resonator lattices can be utilized as a versatile platform for exploring projective symmetry and the associated topological phases, where the flexible manipulation of gauge flux and coupling strength can be simultaneously achieved by engineering the link rings that connect resonant site rings [50–58]. In indirectly coupled microring resonators, the evanescently coupling strength is determined by the gap distance between adjacent rings, while the AGFs are generated by shifting link rings to arouse direction-dependent phases [13,16,59]. Moreover, the resonant frequencies of individual rings can be easily manipulated to introduce the on-site potentials.

\*kshaolin@wit.edu.cn

Therefore, a variety of topological tight-binding lattice models were proposed and demonstrated based on microring resonators, such as the photonic analogy of the quantum Hall insulator [13], quadrupole topological insulators [16,60], quadratic-node semimetals [61], and antihelical edge states [62]. In addition, it is important to note that optics differs from phonics, which seeks to address the impact of fabrication imperfections and disorder in compact photonic devices through the utilization of topological degrees of freedom. The topology provides alternative ways to manipulate and control electromagnetic waves over a broad range of frequencies. Topological photonic systems hold the potential for various applications, such as disorder-robust waveguides, delay lines, optical isolators, and topological lasers [1,2]. Hence the integration of these concepts into the photonic platform is of great importance. Here we utilize microring resonators to construct two-dimensional (2D) rectangle lattices with  $\pi$  flux threading certain plaquettes, formulating projective spatial symmetries. Subsequently, we achieve three kinds of topological phases unique to gauge lattices, including the Möbius topological insulator, graphenelike semimetal, and the Brillouin Klein bottle. We also perform full-wave simulation to verify the theoretical results. The simulated absorption spectra, field distributions, and discussions regarding robustness provide more comprehensive insight into the behavior of the coupled ring resonator arrays. Furthermore, this analysis incorporates all pertinent physical parameters, including refractive indices, ring lengths, and coupling gaps. This approach extends beyond a tight-binding treatment of eigenvalues and eigenvectors, thereby serving as a link to experimental observations. The study is helpful for the design of photonic integrated topological insulators offered by projective symmetry algebra.

## II. MÖBIUS TOPOLOGICAL INSULATOR

We start by investigating a microring array arranged in a 2D rectangular lattice that respects projective translation symmetry. As shown in Fig. 1(a), each unit cell contains four main site rings (in green), which are evanescently coupled to their neighbors via a set of link rings (in gray and red). The resonant frequency of link rings is different from that of the site rings due to an added length used to control the magnitude and phase of effective coupling. The key to achieving projective symmetry is to generate a  $\pi$  flux threading each plaquette, which is equivalent to inserting a negative coupling into each cell. Towards this goal, we horizontally shift a link ring (plotted in red), as illustrated in Fig. 1(b). For clockwise rotation modes, light coupling from the lower to upper site rings along the  $y$  direction experiences a longer propagation distance compared to that from the inverse direction. This yields a direction-dependent coupling phase that leads to AGFs based on the Peierls phase configuration [13]. Thus we can realize an arbitrary gauge flux determined by the shift displacement, with  $\varphi = 2n_{\text{eff}}k_0\Delta x$ , where  $\Delta x$ ,  $k_0$ , and  $n_{\text{eff}}$  denote the shift displacement, the wave vector in vacuum, and the effective refractive index of the ring waveguide, respectively. Furthermore, the magnitude of coupling is tunable by the gap distance between site and link rings, either by deforming the link rings or by changing the distance directly, as shown in Figs. 1(c) and 1(d). The former method has the advantage of

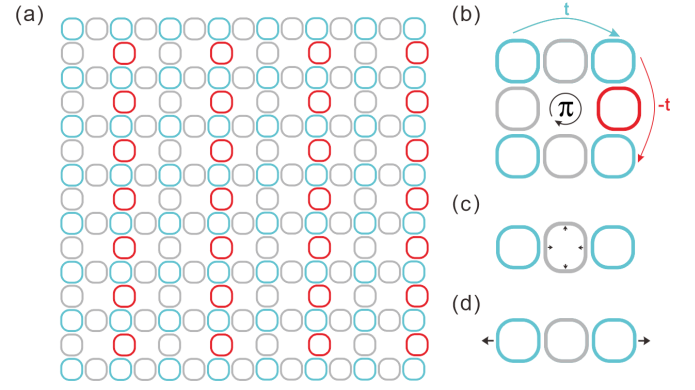


FIG. 1. Schematic diagram of the microring array and the coupling modules. (a) Structural model of the microring array under a square lattice with projective translation symmetry. The green ring indicates the main site rings. The gray (red) indicates connecting rings with positive (negative) coupling. (b) The unit cell with  $\pi$  flux. The red link ring is shifted to create a negative coupling. (c,d) plot the design of link rings to control the coupling strength between the two main rings.

preserving the lattice period, which is useful for implementing different forms of dimerization.

In the absence of AGFs, the two primary translation operators for a rectangle lattice,  $L_x$  and  $L_y$ , should commute with each other  $[L_x, L_y] = 0$ , which is the fundamental representation in an ordinary crystal lattice. However, they develop into projective symmetry since each plaquette carries a  $\pi$  flux [30]. This is because the wave function acquires an additional  $\pi$  phase during the transformation. The algebra of the two symmetries is expressed in the anticommutation relation,

$$\{\hat{L}_x, \hat{L}_y\} = 0, \quad (1)$$

with

$$\hat{L}_x = GL_x = \begin{pmatrix} 0 & 1 & 0 & 0 \\ e^{ik_x} & 0 & 0 & 0 \\ 0 & 0 & 0 & -1 \\ 0 & 0 & -e^{ik_x} & 0 \end{pmatrix},$$

$$\hat{L}_y = L_y = \begin{pmatrix} 0 & 0 & 1 & 0 \\ 0 & 0 & 0 & 1 \\ e^{ik_y} & 0 & 0 & 0 \\ 0 & e^{ik_y} & 0 & 0 \end{pmatrix}, \quad (2)$$

where  $G$  denotes a gauge transformation. An immediate consequence of projective symmetry is that each band must be doubly degenerated at a single momentum. Furthermore, the system also respects time-reversal symmetry for equivalent spatial space due to  $\pm\pi$  yielding the same gauge flux. Therefore, there must be a fourfold Dirac point enforced at the  $M$  point ( $k_x = \pi$ ,  $k_y = \pi$ ) [30]. This observation can also be derived from the periodic eigenvalues as

$$E_{\pm} = \pm t \sqrt{2(\cos k_x + \cos k_y + 2)}, \quad (3)$$

where  $t$  represents the coupling coefficients and  $k_x(k_y)$  represents Bloch momentum along the  $x(y)$  direction. It is evident that the eigenvalues coalesce to  $E = 0$  at the  $M$  point ( $k_x = \pi$ ,  $k_y = \pi$ ).

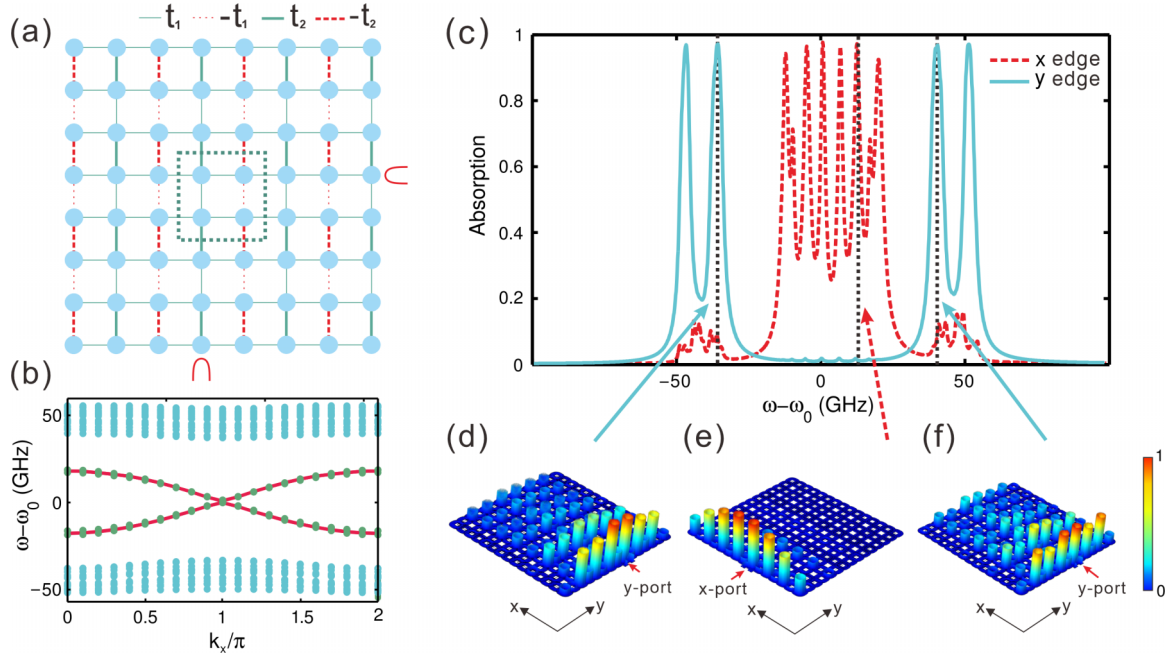


FIG. 2. Möbius topological insulator based on microring resonators. (a) The diagram of the lattice model and the location of excitation ports. (b) Simulated band structure for Möbius topological insulator. (c) Absorbance spectra of Möbius insulators excited from the  $x$  edge and  $y$  edge. The spatial gaps are  $g_1 = 0.35 \mu\text{m}$  and  $g_2 = 0.26 \mu\text{m}$ . (d–f) The field distributions ( $|\mathbf{E}|$ ) at different frequencies with  $\omega - \omega_0 = -35.7, 13.4, \text{ and } 41.4 \text{ GHz}$ .

The emergence of the fourfold Dirac point is a unique feature of the projective symmetry group that does not require additional point group symmetries. Moreover, this Dirac point has a unique topological property that gives rise to novel topological insulators for different coupling configurations. To explore this, we begin by investigating the Möbius topological insulator by breaking  $L_y$  symmetry while preserving

$L_x$  symmetry. The corresponding lattice model is illustrated in Fig. 2(a), where there is an alternating coupling strength along the  $y$  direction but it is uniform in the  $x$  direction. The thick and thin lines depict strong and weak coupling coefficients, respectively, which can be achieved by adjusting the gap distance between site and link rings along the  $y$  direction. The Hamiltonian of the proposed system is given by

$$H_M = \begin{pmatrix} 0 & 0 & t_1 + t_1 e^{-ik_x} & -t_1 - t_2 e^{ik_y} \\ 0 & 0 & -t_1 - t_2 e^{-ik_y} & t_1 + t_1 e^{ik_x} \\ t_1 + t_1 e^{ik_x} & -t_1 - t_2 e^{ik_y} & 0 & 0 \\ t_1 + t_2 e^{-ik_y} & t_1 + t_1 e^{-ik_x} & 0 & 0 \end{pmatrix}, \quad (4)$$

where  $t_1$  and  $t_2$  denote the intra- and intercouplings along the  $y$  direction, and the coupling strength along the  $x$  direction is also  $t_1$ .

We conducted a full-wave simulation based on the finite element method using COMSOL to work out the band structure of a strip lattice. In this simulation, the width and the refractive index of the waveguide core are fixed at  $w = 0.27 \mu\text{m}$  and  $n_{\text{core}} = 3$ , respectively. The cladding material is assumed to be air for simplicity. The waveguide only supports a single TE-polarized mode with an effective refractive index  $n_{\text{eff}} = 2.39$  at a wavelength  $\lambda = 1.55 \mu\text{m}$ . The vertical and horizontal lengths of the site rings are  $L_1 = L_2 = 8 \mu\text{m}$  with a fillet radius  $r = 3 \mu\text{m}$ . With these parameters, the resonant frequency of a single site ring is calculated to be  $\omega_0 = (196.05 + 6i \times 10^{-4}) \text{ THz}$  with a small imaginary part induced by radiation loss. The extra circumference of the link rings is set to be  $\Delta L = \pi / (n_{\text{eff}} k_0) = 0.32 \mu\text{m}$  to fulfill the antiresonant condition. The gap distances between

site and link rings for weak and strong couplings are chosen as  $g_1 = 0.35 \mu\text{m}$  and  $g_2 = 0.26 \mu\text{m}$ , corresponding to  $t_1 = 8.9 \text{ GHz}$  and  $t_2 = 44 \text{ GHz}$ , respectively. The shift displacement of the link ring is  $\Delta x = 0.16 \mu\text{m}$  to generate a  $\pi$  flux in each plaquette. Figure 2(b) shows the resulting band structure for open boundary conditions (OBCs) along the  $y$  direction and the periodic boundary condition (PBC) along the  $x$  direction. There are 16 site rings along the  $y$  direction. Due to the dimerization, the Dirac point is destroyed, and the band structures are open. In the band gap, two twisted bands appear without touching the bulk bands, which are topological edge modes and referred to as the Möbius topological insulator. Each edge band is twofold degenerate as a result of projective symmetry. Moreover, the two bands cross at  $k_x = \pi$  and run parallel to the horizontal at  $k_x = 0, 2\pi$ , indicating that the edge bands have a  $4\pi$  periodicity as opposed to the general Bloch bands, which only have a  $2\pi$  periodicity.

The Möbius twisted edge bands can be understood using a tight-binding model. Considering  $[\hat{L}_x, H] = 0$ , the Hamiltonian of the proposed system can be block diagonalized in the eigenspace of projective translation operator  $\hat{L}_x$ ,

$$UH_M U^\dagger = \begin{pmatrix} h_1(\mathbf{k}) & 0 \\ 0 & h_2(\mathbf{k}) \end{pmatrix}, \quad (5)$$

with

$$h_{1,2}(\mathbf{k}) = \begin{pmatrix} 0 & t_1 + t_2 e^{ik_y} \\ t_1 + t_2 e^{-ik_y} & 0 \end{pmatrix} \pm 2t_1 \cos(k_x/2). \quad (6)$$

Each block corresponds to a Su-Schrieffer-Heeger (SSH) model with alternating couplings  $t_1$  and  $t_2$  and an additional on-site term  $2t_1 \cos k_x$ . Therefore, at a fixed momentum  $k_x$ , each block will support two topological edge modes as  $t_1 < t_2$  with energies given by

$$E_{\text{edge}}^\pm = \pm t_1 \cos(k_x/2). \quad (7)$$

It is apparent that the band structure for edge modes experiences a  $4\pi$  periodicity and they cross each other at  $k_x = \pi$ . In Fig. 2(b), the circles and lines represent the numerical and theoretical results, which are in good agreement with each other.

The Möbius edge bands can be reflected further from absorption spectra and field distributions by extra excitation, which can be regarded as an experiment signature for observing Möbius topological insulators. To achieve this, we added two extra ports at the  $x$  and  $y$  edges of the 2D array, with their locations indicated in Fig. 2(a). Figure 2(c) displays the absorption spectra of an  $8 \times 8$  array of resonant cavities. When light is launched from the  $y$ -edge port, two separate resonant peaks appear near  $\omega - \omega_0 = \pm 50$  GHz, corresponding to two bulk bands. Here the maximum value of the absorption peak is affected by the gap between the port and the array, but different gaps do not have a significant effect on the shape of the absorption line. The amplitudes of absorption peaks are strongly dependent on the gap distances, which will determine whether the external port and the arrays are over-, under-, or critically coupled. As shown in Fig. 2(c), the amplitudes of absorption peaks of the bulk band can reach unity as the gap  $g_x(g_y) = 0.38 \mu\text{m}$ , which corresponds to the critical coupling of edge bands. The deviation from this gap distance will lead to lower peaks. We note that the absorbance spectra within the  $x$ -periodic edge band gap of the Möbius insulator are fluctuating. This is related to the number of edge loops. As the number of rings becomes larger, the number of peaks also becomes larger. We depict two typical field distributions ( $|\mathbf{E}|$ ) for these bands in Figs. 2(d) and 2(f), where light is distributed throughout the arrays, revealing their bulk nature. On the other hand, a remarkable peak appears near  $\omega_0$  when light is injected from the  $x$  edge. This resonant peak corresponds to edge modes, where the fields are confined at the boundary, as depicted in Fig. 2(e). The intensity of the edge state decreases when it reaches the corner of the lattice. Such field distribution may be caused by the interference between propagating waves and the reflected wave from the corner. The resonant peak frequencies for both bulk and edge modes are consistent with the eigenfrequencies shown in Fig. 2(b). The edge modes that appear at the  $x$  or  $y$  directions are determined by the dimerization of spatial spacing. Here, we dimerized the

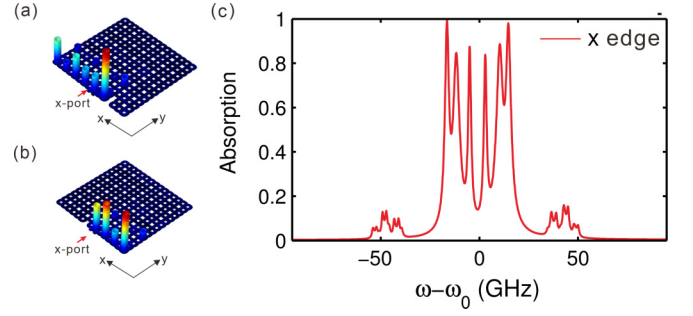


FIG. 3. Robustness of Möbius edge modes. (a,b) The field distribution after removing one of the connecting rings or the main ring. (c) The absorption spectrum calculated after removing one ring.

spacing along the  $y$  direction and thus the edge modes appear at the  $x$  direction. We emphasize that each edge band is doubly degenerated, with the edge states of one band localized at the top boundary and the other at the bottom. In Fig. 2, we launch light from the bottom, which only stimulates the edge states at the bottom.

To test the robustness of the Möbius edge states, we removed a connecting ring and a main ring from the edge for two cases. We excited the system at the same frequency as in Fig. 2(e). As shown in Figs. 3(a) and 3(b), the Möbius edge states persist. Subsequently, we calculated the absorption spectrum after removing the ring and found that the shape of the spectrum did not change significantly compared to that in Fig. 2(c). The results indicate the edge states are robust against the defect. Since Möbius edge states only appear along the  $x$  edge here, we specifically calculated the absorption spectrum for the  $x$ -edge excitation.

### III. GRAPHENELIKE SEMIMETAL

We have utilized a distinct dimerization pattern to disrupt both  $L_x$  and  $L_y$  symmetries, ultimately eliminating the fourfold Dirac point and arousing a pair of twofold Weyl points along the  $k_x$  direction [32]. These two points possess nontrivial topological charges, marked by a quantized Berry phase of  $\pi$  along an enclosed loop and protected by  $\mathcal{PT}$  symmetry. Similar to graphene with a hexagonal lattice, they create a topological flat band of edge modes that connect the projection of the two Weyl points [32,47]. The diagram of the lattice model is shown in Fig. 4(a), where the thick and thin lines indicate the strong and weak coupling coefficients, respectively. This fluctuation in coupling strength among different rows can be achieved by altering link rings to modify gap distances while preserving the lattice constant. To clarify, the position of the primary site rings remains unaffected, as explained in Fig. 1(c).

The corresponding tight-binding Hamiltonian is given by

$$H_G = \begin{pmatrix} 0 & 0 & t_1 + t_1 e^{-ik_x} & t_1 + t_2 e^{ik_y} \\ 0 & 0 & -t_2 - t_1 e^{-ik_y} & t_1 + t_1 e^{ik_x} \\ t_1 + t_1 e^{ik_x} & -t_2 - t_1 e^{ik_y} & 0 & 0 \\ t_1 + t_2 e^{-ik_y} & t_1 + t_1 e^{-ik_x} & 0 & 0 \end{pmatrix} \quad (8)$$

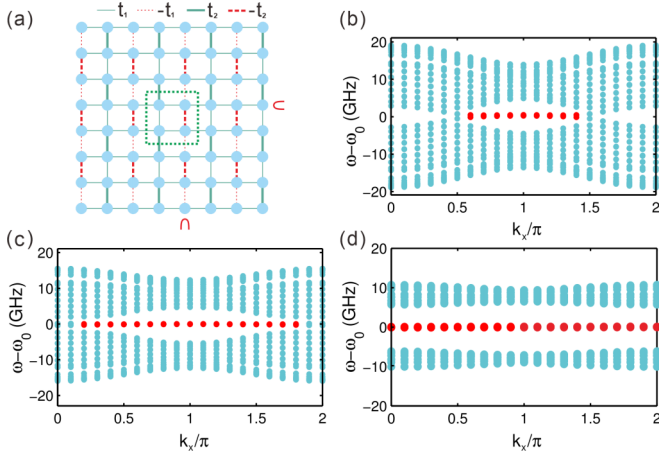


FIG. 4. Graphenelike semimetal and the flat-band topological edge modes based on microring array. (a) The tight-binding lattice and scheme of excitation ports. (b–d) are the simulated band structures for spacing  $g_2 = 0.38, 0.40,$  and  $0.46 \mu\text{m}$ , respectively. In all cases, the other spacing is fixed at  $g_1 = 0.35 \mu\text{m}$ .

as the fourfold degenerate point locates at  $(k_x = \pi, k_y = \pi)$ . After introducing the dimerization, the resulting Weyl points appear at momentum  $(\pm K_x, \pi)$ . The location of momentum  $K_x$  is determined by the characteristic polynomial and is derived as

$$K_x = \pm 2 \arccos\left(\frac{t_2 - t_1}{2t_1}\right). \quad (9)$$

The simulated band structures for OBC along the  $x$  boundary and PBC along the  $y$  direction are presented in Fig. 4(b). In the simulation, the gap distances for the strong and weak couplings are  $g_1 = 0.35 \mu\text{m}$  and  $g_2 = 0.38 \mu\text{m}$ . The length of link rings is adjusted to be  $L_1 = 7.4 \mu\text{m}$  and  $L'_1 = 8.6 \mu\text{m}$ , while their widths are adjusted to keep the total circumference constant and ensure an antiresonant condition for the link rings. The resulting weak and strong couplings are figured out to be  $t_1 = 4 \text{ GHz}$  and  $t_2 = 8.9 \text{ GHz}$ , respectively. The energy band exhibits a boundary band that is relatively flat (red dots) at frequency  $\omega = \omega_0$ , connecting the nodes on both sides ( $K_x \approx 2\pi/3$  and  $K_x \approx 4\pi/3$ ), resulting in a semimetal phase. By increasing the gap distance to  $g_2 = 0.4 \mu\text{m}$ , the difference between the strong and weak coupling coefficients is enhanced, leading to an enlarged range of flat band in the Brillouin zone, as shown in Fig. 4(c). Further increasing  $g_2$ , when  $t_2 > 3t_1$  according to Eq. (9), the two Weyl points vanish, and the flat band extends throughout the Brillouin zone, as shown in Fig. 4(d).

To further investigate the property of the flat band, we likewise reflect it by the absorption spectra. There are two additional ports on the  $x$  edge and  $y$  edge of the 2D microring array as depicted in Fig. 4(a). Figure 5(a) presents the absorption spectra with the red and green lines denoting the excitation from the  $x$  and  $y$  edges, respectively. The distance between the array and two ports is equal, with  $g_x = g_y = 0.42 \mu\text{m}$ . When the light is incident from the  $y$ -edge port, two resonant peaks near  $\omega - \omega_0 = \pm 10 \text{ GHz}$  are observed, corresponding to the bulk band. The field distributions at two typical frequencies for the resonant peaks are shown in

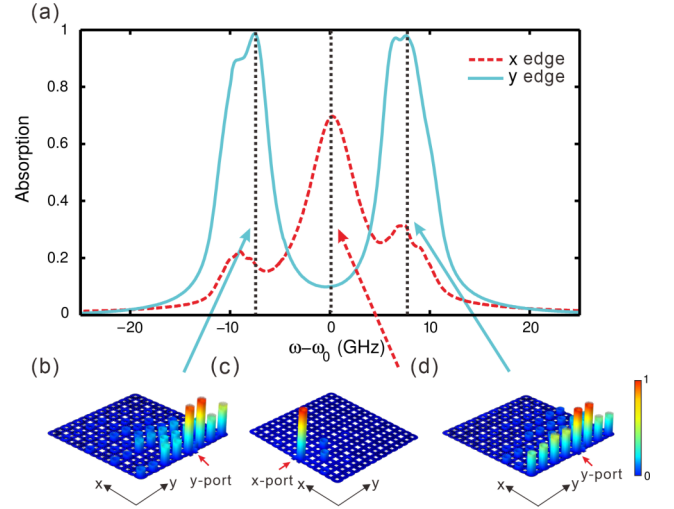


FIG. 5. Excitation of flat-band topological edge modes in microring array. (a) Absorption spectra for excitation from the  $y$ -axis and  $x$ -axis ports as  $g_1 = 0.35 \mu\text{m}$  and  $g_2 = 0.46 \mu\text{m}$ . (b–d) are the field distributions ( $|\mathbf{E}|$ ) for bulk and boundary modes at the absorption peaks  $\omega - \omega_0 = -7.5, 0,$  and  $7.7 \text{ GHz}$ , respectively.

Figs. 5(b) and 5(d), where the fields are distributed into the center of the array, indicating their bulk nature. On the other hand, when the light is illuminated from the  $x$ -edge port, a significant resonant peak appears near  $\omega_0$ , arising from the flat band of the edge modes. The field distribution is shown in Fig. 5(c), where the fields are confined to the site rings near the incidence, indicating their compact nature which is useful to decrease the array size along the  $x$  direction. It does not matter which ring is coupled to the external port. The topological flat mode can be excited from any rings at the  $x$  edge. This is because the edge states corresponding to the flat band become compacted states. The frequencies of the resonant peaks for the bulk and the edge modes are consistent with the eigenfrequency spectra shown Fig. 4(d).

We also tested the robustness of the flat-band edge modes, as shown in Fig. 6. We removed one connecting ring or the main ring from the edge, as shown in Figs. 6(a) and 6(b). We excited it at the same frequency as in Fig. 5(c) and present the corresponding field distribution, where the fields are still confined near the port, confirming the persistence of the edge

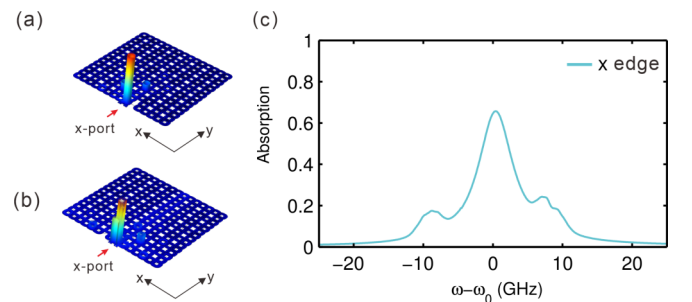


FIG. 6. Robustness of flat-band edge states. [(a), (b)] The field distribution of edge mode after removing one of the connecting rings or the main ring. (c) The absorption spectrum after removing one ring.

states. Subsequently, we calculated the absorption spectrum after removing the ring and found that the shape of the spectrum did not change significantly compared to that in Fig. 5(a), indicating the flat edge band is still present.

#### IV. BRILLOUIN KLEIN BOTTLE

We now investigate the Klein bottle in the Brillouin zone resulting from projection symmetry in microring lattices. In typical lattices, their Brillouin zones in reciprocal space form a torus. However, under a special flux configuration, the Brillouin zone can be deformed into a Klein bottle due

$$H_0 = \begin{pmatrix} \Delta\varepsilon & t_{x1} + t_{x2}e^{-ik_x} & t_{y1} + t_{y2}e^{-ik_y} & 0 \\ t_{x1} + t_{x2}e^{ik_x} & \Delta\varepsilon & 0 & t_{y1} - t_{y2}e^{-ik_y} \\ t_{y1} + t_{y2}e^{ik_y} & 0 & -\Delta\varepsilon & t_{x2} + t_{x1}e^{-ik_x} \\ 0 & t_{y1} - t_{y2}e^{ik_y} & t_{x2} + t_{x1}e^{ik_x} & -\Delta\varepsilon \end{pmatrix}, \quad (10)$$

where the lattice constants are assumed to be 1,  $t_{xi}$  and  $t_{yi}$  denote coupling coefficients indicated in Fig. 7(a), and  $\Delta\varepsilon$  is the detuning of on-site potentials. In the gauge lattice, the mirror symmetry  $\hat{M}_x$  and the translation symmetry  $\hat{L}_y$  become anticommutative, that is,

$$\{\hat{M}_x, \hat{L}_y\} = 0. \quad (11)$$

This occurs due to the requirement of an additional gauge transformation for mirror symmetry  $\hat{M}_x = G\hat{M}_x$  in the presence of  $\pi$  flux [46]. In momentum space, if we consider the operator  $\hat{L}_y = e^{ik_y b}$  with  $b$  denoting the lattice constant along the y

to a projective representation of the algebra between mirror and translation symmetries, resulting in the nonsymmorphic momentum-space glide reflection [46,48,49]. The proposed lattice model is depicted in Fig. 7(a), where the array has alternating zero and  $\pi$  fluxes in adjacent rows. In the lattice, the green and red lines represent positive and negative couplings, respectively, and the thick and thin lines depict the strong and weak couplings, respectively. The two kinds of gauge flux can be obtained by shifting the link rings, while the magnitude of effective coupling between the main rings is similarly controlled by compressing (stretching) the link rings. The Hamiltonian is given by the following equation,

direction, an immediate consequence of Eq. (11) is

$$\hat{M}_x e^{ik_y b} \hat{M}_x = -e^{ik_y b} = e^{i(k_y + G_y/2)b}, \quad (12)$$

with  $G_y$  depicting the length of the reciprocal lattice. As a result, mirror symmetry must contain a half translation, regarded as momentum-space glide reflection, which imposes constraints on the Hamiltonian given by

$$\hat{M}_x H(k_x, k_y) \hat{M}_x = H(-k_x, k_y + \pi). \quad (13)$$

Thus the energy at momentum  $(k_x, k_y)$  is equal to that at  $(-k_x, k_y + \pi)$ , leading to the division of the Brillouin zone into two parts ( $\tau_{1/2}$  and  $\bar{\tau}_{1/2}$ ), as shown in Fig. 7(b), whereby only one region is independent. The fundamental domain of momentum space is now half of the Brillouin zone, and the Brillouin zone only has a period  $\pi$  in the y direction, culminating in the formation of the Klein bottle.

We performed full-wave simulations on a microring lattice to verify this property. In the simulation, we vary the widths of the upper and lower main rings of the unit cell to be 8.0001 and 7.999  $\mu\text{m}$ , respectively, to introduce an on-site energy offset  $\Delta\omega = 3$  GHz. The on-site detuning is  $\Delta\varepsilon = 8.9$  GHz, and the effective coupling coefficients are  $t_{x1} = 8.9$  GHz,  $t_{y2} = 15$  GHz,  $t_{y1} = 18.5$  GHz, and  $t_{x2} = 36.5$  GHz. The corresponding coupling distances between the main ring and the connecting ring are  $g_{x1} = 0.35$   $\mu\text{m}$ ,  $g_{y2} = 0.32$   $\mu\text{m}$ ,  $g_{y1} = 0.31$   $\mu\text{m}$ , and  $g_{x2} = 0.27$   $\mu\text{m}$ , respectively. Figures 7(c) and 7(d) depict two typical energy bands as a function of momentum  $k_x$  for  $k_y = -0.9\pi$  and  $0.1\pi$ , respectively. Upon comparing the two bands, they are identical when reflected with respect to the momentum  $k_x = 0$ . This confirms the nonsymmorphic behavior in momentum space, meaning that the spectrum at  $(k_x, k_y)$  is equivalent to that of  $(-k_x, k_y + \pi)$ .

The fraction of the Brillouin zone changes the fundamental domain for topological classification, extending beyond the Chern number and resulting in a Klein bottle topological insulator [46]. Figure 8(a) plots the band structure for a ribbon with OBC along the x direction and PBC along the y direction, where the coupling coefficients and the coupling distances between the main ring and the connecting ring are consistent

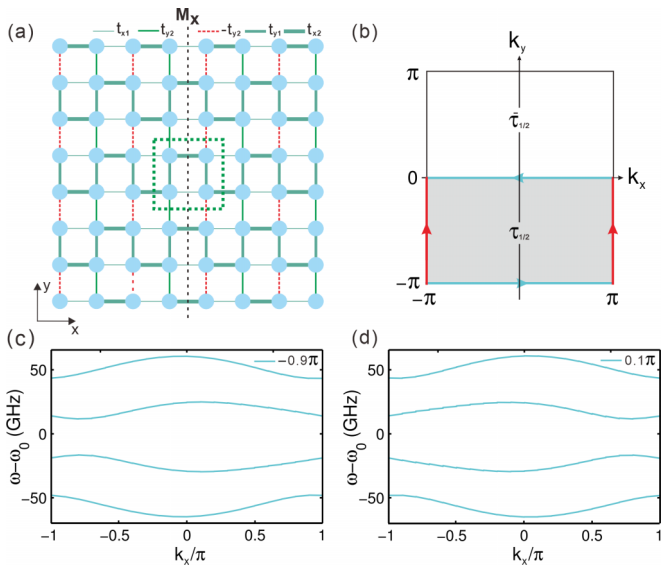


FIG. 7. Fraction of Brillouin zone from projective mirror symmetry based on a microring array. (a). Lattice model for the Brillouin Klein bottle. (b) The fundamental domain of the Brillouin zone is  $\tau_{1/2}$ . (c, d) are the simulated band structure for two associated momenta as  $k_y = -0.9\pi$  and  $k_y = 0.1\pi$ . This confirms that the spectrum at  $(k_x, k_y)$  is equivalent to the spectrum at  $(-k_x, k_y + \pi)$ .

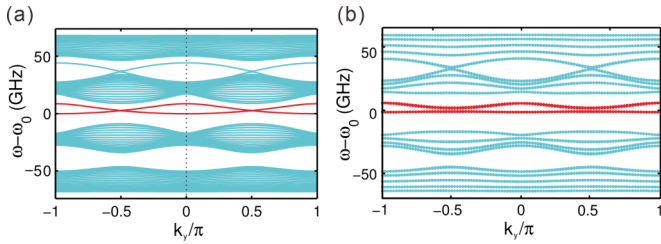


FIG. 8. The Klein bottle topological insulator. (a) The band structure of a strip computed using the tight-binding model. (b) Simulated topological band structure of the Klein bottle.

with the energy band diagrams obtained in Figs. 7(c) and 7(d). The structure is topologically nontrivial as the intermediate band gap is opened and two edge bands plotted in red appear near zero energy. This Klein bottle insulator has unique properties. The bands are only independent in the range  $k_y \in (0, \pi]$  and that in  $k_y \in (-\pi, 0]$  can be obtained by shifting the spectra of  $k_y \in (0, \pi]$  by  $\pi$ . Furthermore, these edge bands can be completely detached from the bulk band. Additionally, we performed full-wave simulations using COMSOL. The numerical band structure is shown in Fig. 8(b), which is consistent with the theoretical results in Fig. 8(a).

## V. CONCLUSIONS

In conclusion, we have investigated three distinct topological phases by leveraging gauge fields and projective symmetry algebra in a photonic platform consisting of arrays of microring resonators. By exploring the projective translation symmetry on a rectangle lattice, we achieve a Möbius topological insulator and a graphenelike semimetal by employing different spatial dimerization configurations. Moreover, we

have examined the projective representation between mirror and translation symmetries, resulting in a Klein bottle topological insulator, where the band structures of topological edge modes exhibit a doubled period in the Brillouin zone. However, it is important to note that the proposed microring lattices are limited to two dimensions. Expanding these topological phases into three dimensions can be achieved by incorporating the pseudospin of clockwise and counterclockwise modes in each resonator or by employing synthetic frequency dimensions through dynamic modulation. This expansion into the third dimension opens up possibilities for a wider range of topological phases originating from projective symmetry in photonic lattices, such as the spinful topological phases and high-order topological phases. Furthermore, the combination of projective symmetry groups and non-Hermitian topological physics remains an intriguing and unexplored topic. The interaction between these areas holds great potential for the development of novel photonic topological insulators and new approaches to steering the transmission of light.

## ACKNOWLEDGMENTS

The work is supported by the Guangdong Major Project of Basic and Applied Basic Research (Grant No. 2019B030302003); the National Natural Science Foundation of China (Grant No. 12204363); the Natural Science Foundation of Hubei Province, China (Grant No. 2022CFB753); the Natural Science Foundation of Zhejiang province, China (Grant No. LQ23A040001); the Open Foundation project of Hubei Provincial Key Laboratory of Optical Information and Pattern Recognition, Wuhan Institute of Technology (Grant No. 202203). The 15th Graduate Education Innovation Fund of Wuhan Institute of Technology (Grant No. CX2023275).

- 
- [1] T. Ozawa *et al.*, Topological photonics, *Rev. Mod. Phys.* **91**, 015006 (2019).
  - [2] A. B. Khanikaev and G. Shvets, Two-dimensional topological photonics, *Nat. Photonics* **11**, 763 (2017).
  - [3] W. Zhang, X. Chen, and F. Ye, Plasmonic topological insulators for topological nanophotonics, *Opt. Lett.* **42**, 4063 (2017).
  - [4] L. Qi, G.-L. Wang, S. Liu, S. Zhang, and H.-F. Wang, Engineering the topological state transfer and topological beam splitter in an even-sized Su-Schrieffer-Heeger chain, *Phys. Rev. A* **102**, 022404 (2020).
  - [5] D. Smirnova, D. Leykam, Y. Chong, and Y. Kivshar, Nonlinear topological photonics, *Appl. Phys. Rev.* **7**, 021306 (2020).
  - [6] X.-X. Wang, Z. Guo, J. Song, H. Jiang, H. Chen, and X. Hu, Unique Huygens-Fresnel electromagnetic transportation of chiral Dirac wavelet in topological photonic crystal, *Nat. Commun.* **14**, 3040 (2023).
  - [7] N. Fu, Z. Fu, H. Zhang, Q. Liao, D. Zhao, and S. Ke, Topological bound modes in optical waveguide arrays with alternating positive and negative couplings, *Opt. Quantum Electron.* **52**, 61 (2020).
  - [8] S. Mandal, R. Banerjee, and T. C. H. Liew, From the topological spin-Hall effect to the non-Hermitian skin effect in an elliptical micropillar chain, *ACS Photonics* **9**, 527 (2022).
  - [9] W. Liu, C. Wu, Y. Jia, S. Jia, G. Chen, and F. Chen, Observation of edge-to-edge topological transport in a photonic lattice, *Phys. Rev. A* **105**, L061502 (2022).
  - [10] B. Ren, H. Wang, M. R. Belić, Y. Li, X. Zhu, and Y. Zhang, Zero-energy edge states and solitons in strained photonic graphene, *Phys. Rev. A* **107**, 043504 (2023).
  - [11] S. Ma, B. Yang, and S. Zhang, Topological photonics in metamaterials, *Photonics Insights* **1**, R02 (2022).
  - [12] Z.-Q. Jiao *et al.*, Experimentally detecting quantized Zak phases without chiral symmetry in photonic lattices, *Phys. Rev. Lett.* **127**, 147401 (2021).
  - [13] M. Hafezi, S. Mittal, J. Fan, A. Migdall, and J. M. Taylor, Imaging topological edge states in silicon photonics, *Nat. Photonics* **7**, 1001 (2013).
  - [14] B. Xie, H. Liu, H. Wang, H. Cheng, J. Tian, and S. Chen, A review of topological semimetal phases in photonic artificial microstructures, *Front. Phys.* **9**, 771481 (2021).

- [15] Y. Zhang, D. Bongiovanni, Z. Wang, X. Wang, S. Xia, Z. Hu, D. Song, D. Jukić, J. Xu, R. Morandotti, H. Buljan, and Z. Chen, Realization of photonic  $p$ -orbital higher-order topological insulators, *eLight* **3**, 5 (2023).
- [16] S. Mittal, V. V. Orre, G. Zhu, M. A. Gorlach, A. Poddubny, and M. Hafezi, Photonic quadrupole topological phases, *Nat. Photonics* **13**, 692 (2019).
- [17] D. Leykam, K. Y. Bliokh, C. Huang, Y. D. Chong, and F. Nori, Edge modes, degeneracies, and topological numbers in non-Hermitian systems, *Phys. Rev. Lett.* **118**, 040401 (2017).
- [18] Q. Yan, B. Zhao, R. Zhou, R. Ma, Q. Lyu, S. Chu, X. Hu, and Q. Gong, Advances and applications on non-Hermitian topological photonics, *Nanophotonics* **12**, 2247 (2023).
- [19] S. Ke, W. Wen, D. Zhao, and Y. Wang, Floquet engineering of the non-Hermitian skin effect in photonic waveguide arrays, *Phys. Rev. A* **107**, 053508 (2023).
- [20] S. Ke, D. Zhao, J. Fu, Q. Liao, B. Wang, and P. Lu, Topological edge modes in non-Hermitian photonic Aharonov-Bohm cages, *IEEE J. Sel. Top. Quantum Electron.* **26**, 1 (2020).
- [21] S. Li, S. Wang, S. Chen, Y. Wu, S. Ke, B. Wang, and P. Lu, Subspace-induced Dirac point and nondissipative wave dynamics in a non-Hermitian optical lattice, *Phys. Rev. A* **105**, 033512 (2022).
- [22] X. Xu, R. Bao, and T. C. H. Liew, Non-Hermitian topological exciton-polariton corner modes, *Phys. Rev. B* **106**, L201302 (2022).
- [23] Y. Song, S. Ke, Y. Chen, and M. Wang, Mode-locking in anti- $\mathcal{PT}$  symmetric frequency lattices, *Appl. Phys. Lett.* **122**, 151106 (2023).
- [24] A. Altland and M. R. Zirnbauer, Nonstandard symmetry classes in mesoscopic normal-superconducting hybrid structures, *Phys. Rev. B* **55**, 1142 (1997).
- [25] A. Kitaev, V. Lebedev, and M. Feigel'man, Periodic table for topological insulators and superconductors, in *Advances in Theoretical Physics: Landau Memorial Conference*, AIP Conf. Proc. No. 1134 (AIP, Melville, NY, 2009), p. 22.
- [26] L. Fu, Topological crystalline insulators, *Phys. Rev. Lett.* **106**, 106802 (2011).
- [27] Y. Liu, S. Leung, F.-F. Li, Z.-K. Lin, X. Tao, Y. Poo, and J.-H. Jiang, Bulk–disclination correspondence in topological crystalline insulators, *Nature (London)* **589**, 381 (2021).
- [28] J.-X. Zhang, M. C. Rechtsman, and C.-X. Liu, Invited article: Topological crystalline protection in a photonic system, *APL Photonics* **1**, 050803 (2016).
- [29] F. Tang, H. C. Po, A. Vishwanath, and X. Wan, Comprehensive search for topological materials using symmetry indicators, *Nature (London)* **566**, 486 (2019).
- [30] Y. X. Zhao, Y.-X. Huang, and S. A. Yang,  $Z_2$ -projective translational symmetry protected topological phases, *Phys. Rev. B* **102**, 161117(R) (2020).
- [31] Y. X. Zhao, C. Chen, X.-L. Sheng, and S. A. Yang, Switching spinless and spinful topological phases with projective  $\mathcal{PT}$  symmetry, *Phys. Rev. Lett.* **126**, 196402 (2021).
- [32] L. B. Shao, Q. Liu, R. Xiao, S. A. Yang, and Y. X. Zhao, The gauge-field extended  $\mathbf{k} \cdot \mathbf{p}$  method and novel topological phases, *Phys. Rev. Lett.* **127**, 076401 (2021).
- [33] S. Longhi, Aharonov–Bohm photonic cages in waveguide and coupled resonator lattices by synthetic magnetic fields, *Opt. Lett.* **39**, 5892 (2014).
- [34] A. M. Marques, J. Mögerle, G. Pelegrí, S. Flannigan, R. G. Dias, and A. J. Daley, Kaleidoscopes of Hofstadter butterflies and Aharonov–Bohm caging from  $2^n$ -root topology in decorated square lattices, *Phys. Rev. Res.* **5**, 023110 (2023).
- [35] Q. Lin and S. Fan, Light guiding by effective gauge field for photons, *Phys. Rev. X* **4**, 031031 (2014).
- [36] L. Yuan, Y. Shi, and S. Fan, Photonic gauge potential in a system with a synthetic frequency dimension, *Opt. Lett.* **41**, 741 (2016).
- [37] W. Song *et al.*, Dispersionless coupling among optical waveguides by artificial gauge field, *Phys. Rev. Lett.* **129**, 053901 (2022).
- [38] G. Pelegrí, A. M. Marques, V. Ahufinger, J. Mompert, and R. G. Dias, Second-order topological corner states with ultracold atoms carrying orbital angular momentum in optical lattices, *Phys. Rev. B* **100**, 205109 (2019).
- [39] C. Chen, L. Qi, K. Hu, J. Cao, W. Cui, S. Zhang, and H. Wang, Magnetic-flux-induced tunable completely flat band and topological nearly flat band in square kagome lattice, *Ann. Phys.* **535**, 2200645 (2023).
- [40] C. Wu, Z. Yang, J. Tang, N. Liu, and G. Chen, Flux-controlled skin effect and topological transition in a dissipative two-leg ladder model, *Phys. Rev. A* **106**, 062206 (2022).
- [41] H. Ye, C. Qin, S. Wang, L. Zhao, W. Liu, B. Wang, S. Longhi, and P. Lu, Reconfigurable refraction manipulation at synthetic temporal interfaces with scalar and vector gauge potentials, *Proc. Natl. Acad. Sci. USA* **120**, e2300860120 (2023).
- [42] H. Xue, Z. Wang, Y.-X. Huang, Z. Cheng, L. Yu, Y. X. Foo, Y. X. Zhao, S. A. Yang, and B. Zhang, Projectively enriched symmetry and topology in acoustic crystals, *Phys. Rev. Lett.* **128**, 116802 (2022).
- [43] T. Li, J. Du, Q. Zhang, Y. Li, X. Fan, F. Zhang, and C. Qiu, Acoustic Möbius insulators from projective symmetry, *Phys. Rev. Lett.* **128**, 116803 (2022).
- [44] C. Jiang, Y. Song, X. Li, P. Lu, and S. Ke, Photonic Möbius topological insulator from projective symmetry in multiorbital waveguides, *Opt. Lett.* **48**, 2337 (2023).
- [45] C.-A. Li, S.-J. Choi, S.-B. Zhang, and B. Trauzettel, Dirac states in an inclined two-dimensional Su-Schrieffer-Heeger model, *Phys. Rev. Res.* **4**, 023193 (2022).
- [46] Z. Y. Chen, S. A. Yang, and Y. X. Zhao, Brillouin Klein bottle from artificial gauge fields, *Nat Commun.* **13**, 2215 (2022).
- [47] F. Gao, Y.-G. Peng, Q.-L. Sun, X. Xiang, C. Zheng, and X.-F. Zhu, Topological acoustics with orbital-dependent gauge fields, *Phys. Rev. Appl.* **20**, 064036 (2023).
- [48] Y.-L. Tao, M. Yan, M. Peng, Q. Wei, Z. Cui, S. A. Yang, and Y. Xu, Higher-order Klein bottle topological insulator in three-dimensional acoustic crystals, [arXiv:2305.09174](https://arxiv.org/abs/2305.09174).
- [49] Y. Wang, C. Zhang, Z. Chen, B. Liang, and Y. Zhao, Chessboard acoustic crystals with momentum-space nonsymmorphic symmetries, [arXiv:2305.07174](https://arxiv.org/abs/2305.07174).
- [50] S. Mittal, J. Fan, S. Faez, A. Migdall, J. M. Taylor, and M. Hafezi, Topologically robust transport of photons in a synthetic gauge field, *Phys. Rev. Lett.* **113**, 087403 (2014).
- [51] S. Longhi, D. Gatti, and G. Della Valle, Non-Hermitian transparency and one-way transport in low-dimensional lattices by an imaginary gauge field, *Phys. Rev. B* **92**, 094204 (2015).



- [52] D. Leykam, S. Mittal, M. Hafezi, and Y. D. Chong, Reconfigurable topological phases in next-nearest-neighbor coupled resonator lattices, *Phys. Rev. Lett.* **121**, 023901 (2018).
- [53] D. Leykam and L. Yuan, Topological phases in ring resonators: Recent progress and future prospects, *Nanophotonics* **9**, 4473 (2020).
- [54] Y. Ao, X. Hu, Y. You, C. Lu, Y. Fu, X. Wang, and Q. Gong, Topological phase transition in the non-Hermitian coupled resonator array, *Phys. Rev. Lett.* **125**, 013902 (2020).
- [55] Z. Lin, L. Ding, S. Ke, and X. Li, Steering non-Hermitian skin modes by synthetic gauge fields in optical ring resonators, *Opt. Lett.* **46**, 3512 (2021).
- [56] S. M. Zhang and L. Jin, Compact localized states and localization dynamics in the dice lattice, *Phys. Rev. B* **102**, 054301 (2020).
- [57] H. S. Xu and L. Jin, Coherent resonant transmission, *Phys. Rev. Res.* **4**, L032015 (2022).
- [58] S.-Y. Chen, C. Jiang, S.-L. Ke, B. Wang, and P.-X. Lu, Suppression of non-Hermitian skin effect via Aharonov-Bohm cage, *Acta Phys. Sin.* **71**, 174201 (2022).
- [59] S. Afzal, T. J. Zimmerling, and V. Van, Topological photonics with microring lattices, in *Silicon Photonics IV*, Topics in Applied Physics Vol. 139, edited by D. J. Lockwood and L. Pavesi (Springer International Publishing, Cham, Switzerland, 2021), pp. 365–397.
- [60] Z. Lin, L. Ding, S. Chen, S. Li, S. Ke, X. Li, and B. Wang, Photonic non-Bloch quadrupole topological insulators in coupled ring resonators, *Phys. Rev. A* **103**, 063507 (2021).
- [61] Z. Gao, H. Zhao, T. Wu, X. Feng, Z. Zhang, X. Qiao, C.-K. Chiu, and L. Feng, Topological quadratic-node semimetal in a photonic microring lattice, *Nat Commun.* **14**, 3206 (2023).
- [62] L. Xie, L. Jin, and Z. Song, Antihelical edge states in two-dimensional photonic topological metals, *Sci. Bull.* **68**, 255 (2023).